



Three-dimensional analysis of shear wave propagation observed by *in vivo* magnetic resonance elastography of the brain [☆]

U. Hamhaber ^{a,*}, I. Sack ^b, S. Papazoglou ^b, J. Rump ^b, D. Klatt ^b, J. Braun ^a

^a Institute of Medical Informatics, Charité – Universitätsmedizin Berlin, Hindenburgdamm 30, D-12203 Berlin, Germany

^b Institute of Radiology, Charité – Universitätsmedizin Berlin, Charitéplatz 1, D-10117, Berlin, Germany

Received 2 March 2006; received in revised form 29 August 2006; accepted 29 August 2006

Abstract

Dynamic magnetic resonance elastography (MRE) is a non-invasive method for the quantitative determination of the mechanical properties of soft tissues *in vivo*. In MRE, shear waves are generated in the tissue and visualized using phase-sensitive MR imaging methods. The resulting two-dimensional (2-D) wave images can reveal in-plane elastic properties when possible geometrical biases of the wave patterns are taken into account. In this study, 3-D MRE experiments of *in vivo* human brain are analyzed to gain knowledge about the direction of wave propagation and to deduce in-plane elastic properties. The direction of wave propagation was determined using a new algorithm which identifies minimal wave velocities along rays from the surface into the brain. It was possible to quantify biases of the elastic parameters due to projections onto coronal, sagittal and transversal image planes in 2-D MRE. It was found that the in-plane shear modulus is increasingly overestimated when the image slice is displaced from narrow slabs of 2–5 cm through the center of the brain. The mean shear modulus of the brain was deduced from 4-D wave data with about 3.5 kPa. Using the proposed slice positions in 2-D MRE, this shear modulus can be reproduced with an acceptable error within a fraction of the full 3-D examination time.

© 2006 Acta Materialia Inc.. Published by Elsevier Ltd. All rights reserved.

Keywords: Magnetic resonance elastography; Brain; 3-D analysis; Direction of shear wave propagation; Shear modulus

1. Introduction

For centuries, palpation has been used as the primary test for pathological tissue change. The sensitivity of the method is based on the mechanical resistance of soft tissue to compression and shear deformations, which varies in orders of magnitude throughout the human body. However, manual palpation is a subjective method limited to soft tissues in the vicinity of the body surface. Therefore, dynamic magnetic resonance elastography (MRE) was developed as a non-invasive method for quantitatively measuring the visco-

elastic properties of human soft tissue *in vivo* [1–10]. In contrast to static MRE, where static or quasi-static tissue deformations are applied, dynamic MRE is based on the application of low-frequency acoustic waves penetrating the tissue of interest. Short dynamic excitation pulses are used in transient dynamic MRE, whereas steady-state dynamic MRE – the subject of this study – uses several motion cycles or continuous excitations. The tissue motion is magnetically encoded in the MR phase signal by synchronously oscillating gradients. The wave images display a phase-difference contrast that is sensitive to deflections smaller than 1 μm . In dynamic MRE, if the direction of wave propagation lies in the image plane and boundary effects and viscosity are negligible, the wavelength of the observed wave patterns is related to the elasticity of the tissue.

Comparisons of dynamic MRE with independent shear modulus-determining methods have shown that MRE provides correct quantities in tissue phantoms [1,11–13].

[☆] This work was presented in parts at the First International Conference on Mechanics of Biomaterials & Tissues.

* Corresponding author. Present address: Charité – Universitätsmedizin Berlin, Campus Benjamin Franklin, Institut für Medizinische Informatik, Hindenburgdamm 30, D-12203 Berlin, Germany. Tel.: +49 30 450 539078; fax: +49 30 450 539901.

E-mail address: uwe.hamhaber@charite.de (U. Hamhaber).

Promising studies have recently shown that MRE is able to quantify elastic parameters in well-shielded organs such as the prostate, kidney and liver, where manual palpation is restricted [14–17].

Dynamic MRE is especially suited for assessing *in vivo* brain elasticities. In contrast to manual examination, application of static MRE and ultrasound elastography, this technique is capable of producing results despite the mechanical shielding of the skull. The feasibility of using MRE to acquire wave images of the brain has been demonstrated by several studies [18–25]. For mechanical excitation of the brain, the entire head is vibrated, causing indirectly induced shear waves. Thus, the full three-dimensional (3-D) wave field has to be acquired to correctly measure the resulting convolute wave vector field in the brain. Despite the ability of MRE to detect all components of the full wave field, most brain MRE studies are, in order to save time, based on the acquisition of the wave field in a single image plane followed by a 2-D shear modulus reconstruction. However, a 2-D projection through a 3-D wave field can yield geometrical biases that can result in misinterpretation of the determined planar shear modulus. It has been shown that even for tissue phantoms with simple geometries the wave-propagation process is truly 3-D and the full 3-D wave field has to be considered for an accurate reconstruction of elasticity images [26]. The full 3-D displacement field is particularly important for the brain – with its complex anatomy, shape and mechanisms of indirect wave excitation – in order to deduce correct elastic coefficients.

Thus, in this study, the wave propagation through the brain of a volunteer was analyzed by measuring all wave field components. Assuming isotropy, the final wave field analysis was restricted to the scalar field of the deflection component that has shown the largest penetration depth of the acoustic waves into the brain. The temporal evolution of this component was acquired and these 4-D data were analyzed using a new algorithm that allows the direction of shear wave propagation to be determined. The algorithm is profile-based and assumes that the minimum wavelength indicates the direction of wave propagation from the origin of the ray [27]. The shear modulus of brain tissue determined via this method is compared with the results of a direct inversion of 2-D data and data given in the literature.

The aim of the present study was, therefore, to characterize the regions with the best correlation between wave propagation and images with a transversal, coronal or sagittal orientation. Within these regions, fast *in vivo* 2-D MRE can then be applied with a minimized error range in order to quantify the shear modulus of brain tissue. This reduction in scan time is a crucial precondition for forthcoming studies of patients suffering from brain diseases.

2. Materials and methods

The methods of our study can be divided into (i) wave generation, (ii) imaging sequence development, (iii) data

acquisition, (iv) data preprocessing and (v) data analysis, which finally results in the determination of wave velocities and directions of wave propagation.

2.1. Wave generation

Mechanical waves were fed into the brain of a healthy volunteer via an electromagnetic actuator attached to a bite bar (Fig. 1). Mechanical excitation was applied at a frequency of 83.33 Hz and resulted in a vibration of the head with deflection amplitudes of about 500 μm . Steady state was achieved by applying 10 wave cycles before the start of motion encoding in the imaging sequence.

2.2. Imaging sequence

A single-shot spin-echo based echo planar imaging (EPI) sequence was implemented, which allowed very fast imaging of wave fields by motion encoding in arbitrary orientations [20] (Fig. 2). The sequence started with a trigger signal to activate a function generator, which produced the AC needed for the mechanical excitation. After an adjustable period of time necessary to achieve a steady-state tissue motion, a fat saturation was applied to avoid signal ghosting from fatty tissues. After generating

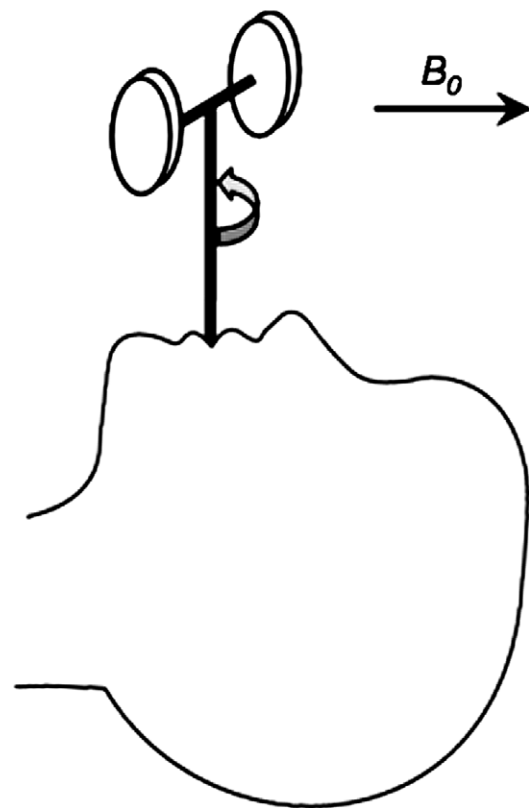


Fig. 1. Outline of electromagnetic actuator functionality. Two coils are attached to each side of the bite bar. A periodical torque is generated around the axis of the actuator as a result of the applied alternating current. This causes a vibrational motion of the head. B_0 indicates the direction of the static magnetic field of the scanner.

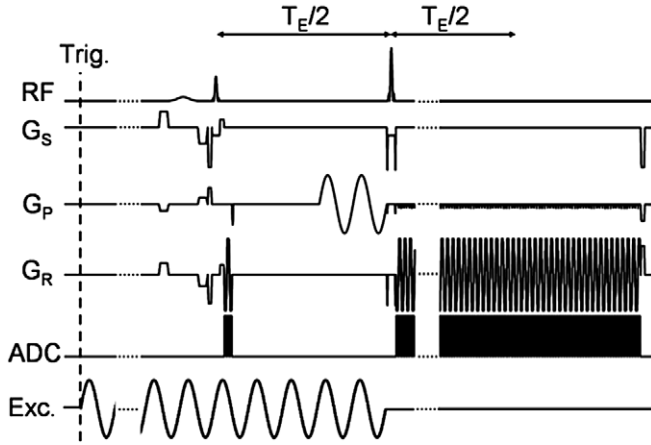


Fig. 2. Diagram of the EPI-MRE sequence. Depicted here is the sequence timing of the radiofrequency pulses (RF), the magnetic field gradients in slice-select, phase-encoding and read-out directions (G_s , G_p , G_r , respectively), the analog-to-digital converter switch (ADC), the AC fed into the electromagnetic actuator (Exc.), and the trigger signal (Trig.). In the example, mechanical vibrations are motion-encoded in the phase-encoding direction (G_p) with two MSG cycles. For the MSG, the number of oscillations, amplitude and frequency can be adjusted. T_E is the time-to-echo of the MR sequence.

transverse magnetization with a 90° radiofrequency (RF) pulse, additional calibration scans were applied in EPI sequences to minimize the appearance of $N/2$ ghosts [28]. The encoding of the periodical tissue deflection was then performed by sinusoidal motion-sensitizing gradients (MSGs) synchronized to the mechanical excitation. Any required motion-encoding direction can be chosen by superpositioning oscillating gradients in all three spatial directions. After motion encoding, a 180° RF pulse was used to invert the spins and create a spin echo. Finally, the complex MR signal was acquired to reconstruct MR magnitude and phase images. The acquisition of one wave image with a 128×128 matrix took about 200 ms.

2.3. Data acquisition

To cover the deflection field $\vec{u}(x, y, z)$ of the 3-D wave propagation in the brain, 23 contiguous 6 mm thick axial slices were acquired (two MSG cycles, amplitude 35 mT m^{-1}) in the anterior–posterior (x), left–right (y) and head–feet (z) directions. Twenty 3-D data sets were acquired at time points equally spaced over one oscillation cycle to measure $u_x(x, y, z, t)$. Other acquisition parameters were a repetition time (TR) of 2 s, a time to echo (TE) of 124 ms, a field of view (FoV) of 192×192 mm, and an in-plane resolution of 1.5×1.5 mm. Using a phase difference image technique [1] to eliminate scanner-dependent effects, total acquisition time for the data set was about 35 min. All examinations were performed on a healthy volunteer using a 1.5 T scanner (Magnetom Sonata, Siemens, Erlangen, Germany) with a standard head coil. The study was approved by our institution's ethics commission.

2.4. Data preprocessing

Phase wraps occurring in acquired phase images were eliminated using a 2-D Flynn's minimum discontinuity method [29]. Residual scanner-dependent phase drifts were eliminated by subtracting two phase images acquired with inverse MSGs. The resulting phase-difference images were arranged in three 3-D arrays for $\vec{u}(x, y, z)$ and one 4-D array for $u_x(x, y, z, t)$. A 4-D filter consisting of an ideal band-pass filter in time and a 3-D Butterworth band-pass filter in space was applied to $u_x(x, y, z, t)$. The temporal filter extracted the harmonic motions equal to the excitation frequency of 83.33 Hz. The spatial filter suppressed waves with wavelengths higher than 19.2 cm and smaller than 0.3 cm.

To obtain the surface points, contour lines of the brain surface were manually segmented from magnitude images.

2.5. Data analysis

As a result of the strong damping of brain tissues the algorithm allows the determination of the direction of wave propagation from spatiotemporal images calculated from profile lines along rays pointing from the surface of an object into its scalar wave deflection field $u(x, y, z, t)$.

Within the algorithm each surface point of the object was successively used as a starting point for an array of discretized rays:

$$\vec{x}_{r,i}(\vec{x}_{s,i}, \varphi, \psi) = \vec{x}_{s,i} + n\Delta d \vec{d}_i^0(\varphi, \psi), \quad (1)$$

where $\vec{x}_{r,i}$ are the rays at the i th surface point, $\vec{x}_{s,i}$ are the positions of the i th surface point, n is the number of samples along a ray, Δd is the sampling distance and $\vec{d}_i^0(\varphi, \psi)$ are normalized direction vectors of rays at the i th surface point dependent on latitude φ and longitude ψ relative to a local spherical reference coordinate system.

The x -directions of the local reference coordinate systems were defined by central rays starting from a particular surface point $\vec{x}_{s,i}$ pointing to the centroid \vec{x}_c of the object (Fig. 3):

$$\vec{d}_i(0^\circ, 0^\circ) = \vec{x}_c - \vec{x}_{s,i}. \quad (2)$$

Arrays of rays were built by spherical sectors around the central rays $\vec{x}_{r,i}(\vec{x}_{s,i}, 0^\circ, 0^\circ)$. The end points of the rays lay on a grid of circles of latitude and meridians of a sphere (Fig. 4). The latitudes and longitudes were in the following ranges:

$$\varphi = -r\Delta\varphi \dots 0^\circ \dots + r\Delta\varphi, \quad (3)$$

$$\psi = -s\Delta\psi \dots 0^\circ \dots + s\Delta\psi, \quad (4)$$

where $\Delta\varphi$, $\Delta\psi$ are increments of latitude and longitude and r , s are whole numbers.

Deflections at the ray points $u(\vec{x}_{r,i}(\varphi, \psi), t)$ were interpolated for all 20 time points. This resulted in a calculated spatiotemporal deflection image for each ray (Fig. 5). These images allowed the shear wave velocities to be

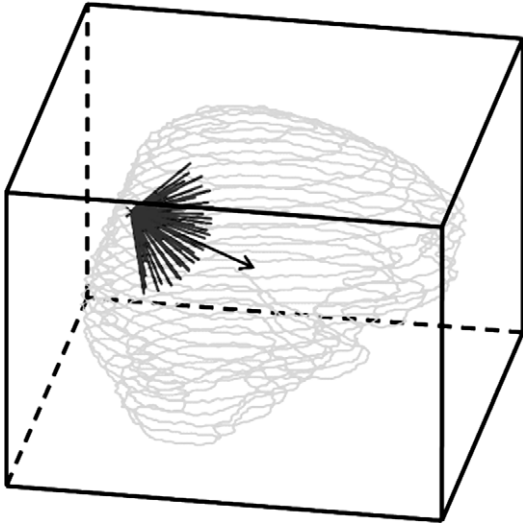


Fig. 3. Segmented brain surface (bright green lines) with analyzed rays (dark gray lines) for a representative surface point. The central ray (arrow) is pointing to the center of the brain.

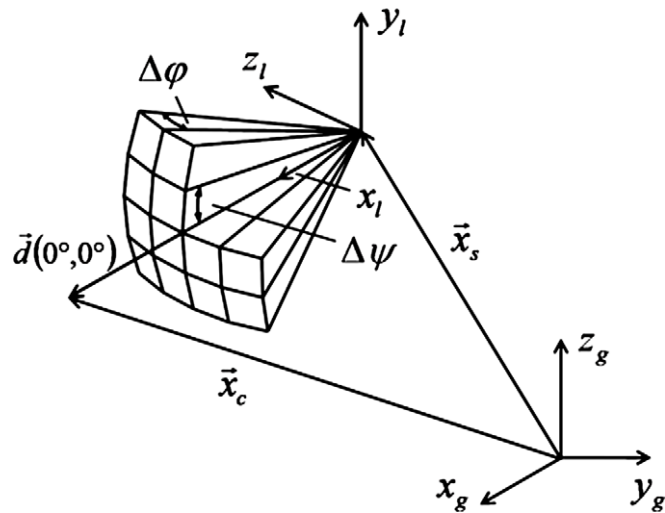


Fig. 4. An array of rays is defined in relation to the direction of a central ray $\vec{d}(0^\circ, 0^\circ)$. Using spherical coordinates, individual rays are positioned by latitudinal $\Delta\varphi$ and longitudinal $\Delta\psi$ increments. A local coordinate system (x_l, y_l, z_l) related to the global coordinate system (x_g, y_g, z_g) is introduced for each surface point.

calculated through a combination of (i) the Canny edge-detection algorithm provided by MATLAB® (MathWorks, Inc., Natick, MA, USA) and (ii) the determination of different edge-building segments according to algorithms by Kovese [30]. If $u(x, y, z, t)$ contains only shear waves and there are no interferences, the slopes of the segments represent shear wave velocities c_t (see Fig. 5):

$$c_t = \frac{\Delta x}{\Delta t} \quad (5)$$

Only segments with positive slopes were considered. Finally, the slopes of all remaining edge segments were

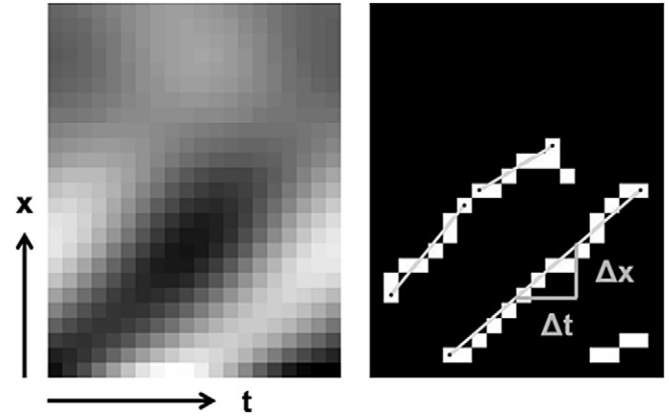


Fig. 5. Left: Example of a spatiotemporal image calculated for a single ray. Right: Automatically detected edges (white) and segments (gray lines) for the spatiotemporal image. Shear wave velocity corresponds to the slope of the segments. All slopes determined for a particular ray were averaged.

averaged to a single shear wave velocity $c_i(\vec{x}_{s,i}, \varphi, \psi)$ for each spatiotemporal image.

This resulted in wave velocity images for each surface point (Fig. 6), where each image point corresponds to a ray in the grid. Median filtering was used for smoothing. The direction $\vec{d}_{\min,i} = \vec{d}_i(\vec{x}_{s,i}, \varphi_c, \psi_c)$ of the ray with the smallest wave velocity $c_{\min,i} = c_i(\vec{x}_{s,i}, \varphi_c, \psi_c)$ was then determined for each spherical sector analyzed.

2.5.1. Evaluation of the algorithm

Three homogeneous spherical software phantoms with geometry (diameter 13 cm) and wave characteristics comparable to the human brain were used for evaluation. For all phantoms, shear waves were simulated (velocity 2.023 m s^{-1} , frequency 83.33 Hz), propagating concentrically from the surface into the center (20 samples over one wave cycle). Three different wave fields were generated: one without damping, one with an attenuation constant of 50 m^{-1} , and one with the damping plus 5% noise (Fig. 7). In total, 164 surface points were analyzed.

With $n = 25$ samples and a sampling distance of $\Delta d = 0.0015 \text{ m}$, the rays had a length of $|\vec{x}_{r,i}| = 0.0375 \text{ m}$. The resulting spatiotemporal images had a matrix size of

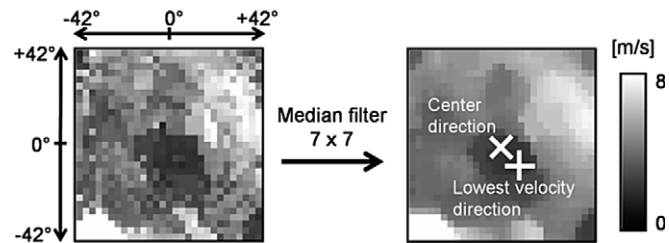


Fig. 6. Left: Example of a wave velocity image for a single surface point. Right: Median filtered velocity image; indicated are the directions to the center of the brain and the calculated direction of lowest wave velocity, which is assumed to be the direction of wave propagation.

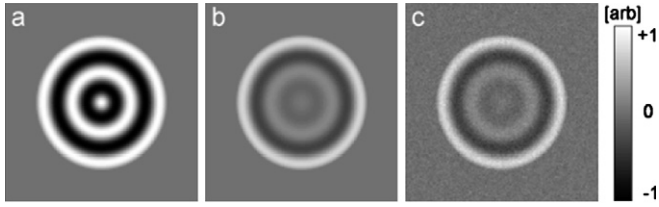


Fig. 7. Wave images positioned at the center of three software phantoms. (a) Ideal phantom without damping. (b) Phantom with damping (attenuation constant 50 m^{-1}). (c) Phantom with damping and additional 5% noise.

25 (spatial) \times 20 (temporal) elements. The aperture angle was 84° in both directions, given in 3° increments for $\Delta\varphi$, $\Delta\psi$, with $r = 29$, $s = 29$, respectively.

The slopes of the detected edge segments in the spatio-temporal images were determined in two ways: (i) from the start and the end point of segments (pp), or (ii) by a linear fit (lf) to all points of a segment. Three 2-D median filters with different window sizes (3×3 , 5×5 and 7×7) were applied prior to the detection of the minimal shear wave velocity.

To analyze the influence of reflections on the algorithm, simulations of spatiotemporal images were performed comprising interferences of incident and reflected waves comparable to the *in vivo* situation in the brain. The spatiotemporal images were simulated for four different cases of gray/white matter impedance differences that were found in the literature. For each case the position of the reflection border was shifted over the entire ray. Temporal and spatial resolutions of the simulated spatiotemporal images were the same as those for the measured data.

2.5.2. Analysis of the brain

The analysis of the brain of a healthy volunteer was restricted to the $u_x(x, y, z, t)$ component which showed the largest penetration depth of the shear waves into the brain tissue. This confinement is justified if isotropy is assumed. The algorithm was applied to 5270 surface points $\vec{x}_{s,i}$. The centroid of the segmented brain \vec{x}_c was calculated assuming that the whole brain was represented by identical point masses at the surface according to

$$\vec{x}_c = \frac{1}{N} \sum_{i=1}^N \vec{x}_{s,i}, \quad (6)$$

where N is the number of surface points.

The slopes of the edge segments were determined by linear fitting. A 7×7 2-D median filter was applied to the resulting velocity images.

The average shear wave velocity of brain tissue and its standard deviation were determined by a fit (curve-fitting toolbox of MATLAB[®]) to the histogram of all determined minimum wave velocities $c_{\min,i}$ using a Gaussian curve according to $g = a \exp(-((x - b)/c)^2)$. The related shear modulus μ was calculated by assuming the material density of the brain to be $\rho = 1000 \text{ kg m}^{-3}$:

$$\mu = \rho c_t^2. \quad (7)$$

The mean deviation angles $\bar{\alpha}_{\text{trans},j}$, $\bar{\alpha}_{\text{cor},j}$ and $\bar{\alpha}_{\text{sag},j}$ between the direction of wave propagation and the corresponding projection onto the j th image plane were calculated for three orthogonal orientations, $\vec{n}_{\text{trans}}^0 = (001)$, $\vec{n}_{\text{cor}}^0 = (100)$ and $\vec{n}_{\text{sag}}^0 = (010)$, using:

$$\sin(\alpha_{\text{plane},i}) = \vec{d}_{\min,i}^0 \cdot \vec{n}_{\text{plane}}^0, \quad (8)$$

where $\alpha_{\text{plane},i}$ is the deviation angle between the direction of wave propagation and the image plane at the i th surface point, $\vec{d}_{\min,i}^0$ is the normalized direction of wave propagation and \vec{n}_{plane}^0 is the normalized normal vector of the image plane.

The deviation angle α_{plane} led to an overestimation factor k for the shear modulus given by

$$G_0 = \frac{1}{\cos^2(\alpha_{\text{plane}})} G_r = k G_r, \quad (9)$$

where G_0 is the overestimated shear modulus and G_r is the real shear modulus.

Minimum averaged overestimation factors \bar{k}_{\min} were determined for the main directions from the mean overestimation factors of $\bar{k}_{\text{trans},j}$, $\bar{k}_{\text{cor},j}$ and $\bar{k}_{\text{sag},j}$ calculated for all slices using Eq. (9). For these orientations, slabs were identified with a maximum error of an additional 10% with respect to the minimal overestimation factors.

The results from the proposed ray analysis were compared with the results from a single-slice Helmholtz inversion [9]. For comparison, the inversion was applied to one single slice and the ray analysis was calculated for the corresponding surface points of this slice. The averaged shear moduli were calculated, whereas the region of average used for the inversion was the same as the region covered by the ray analysis.

Data preprocessing and data analysis were both implemented in MATLAB[®] 7 release 14. The calculation time for each surface point was about 2 min on a 2.66 GHz Intel[®] Pentium[®] 4 processor. The calculation was vectorized for parallel computing.

3. Results

The presentation of the results is divided into (i) evaluation of the proposed algorithm using software phantoms and (ii) analysis of *in vivo* MRE data of the human brain.

3.1. Evaluation of the algorithm

The evaluation of the algorithm is summarized in Table 1. A comparison shows that the presence of damping generally leads to decreased shear wave velocities. The calculation of slopes using only the start and end points (pp) of segments results in a shear wave velocity overestimation of 11% without and 8% with damping (no median filter applied). In this case, added noise reduces the overestimation to 2%. Linear fitting (lf) results in deviations of

Table 1
Averaged minimal shear wave velocities and deviation angles (“mean”) and corresponding standard deviations (“SD”) for wave propagation in phantoms

2-D median filter		No		3 × 3		5 × 5		7 × 7	
		Mean	SD	Mean	SD	Mean	SD	Mean	SD
<i>Minimal shear wave velocity (m s⁻¹)</i>									
No damping	pp	2.24	0.06	2.29	0.08	2.36	0.09	2.42	0.06
	lf	2.01	0.04	2.04	0.04	2.07	0.03	2.10	0.04
Damping	pp	2.19	0.08	2.25	0.08	2.28	0.08	2.30	0.07
	lf	1.95	0.03	1.99	0.05	2.01	0.06	2.03	0.06
Damping + noise	pp	2.07	0.06	2.16	0.06	2.20	0.06	2.22	0.05
	lf	1.95	0.03	1.99	0.04	2.02	0.04	2.03	0.03
<i>Deviation angle (°)</i>									
No damping	pp	3.30	5.86	2.21	3.62	2.90	3.81	2.97	2.88
	lf	3.58	4.47	1.49	2.13	1.24	1.35	1.79	1.57
Damping	pp	6.44	5.85	2.58	4.13	1.72	3.48	1.08	1.80
	lf	5.54	5.79	3.74	4.29	1.96	2.51	1.87	2.18
Damping + noise	pp	6.66	3.94	4.53	3.65	2.20	2.07	1.41	1.40
	lf	6.39	3.76	4.20	2.59	2.20	1.83	1.59	1.26

Wave velocity (2.023 m s⁻¹) and propagation directions (toward the center of the sphere) were exactly specified for all simulated wave fields. Here the deviation angle describes the difference between default and calculated wave propagation direction. Wave fields were simulated without damping (“no damping”), with an attenuation constant of 50 m⁻¹ (“damping”) and with damping plus 5% noise relative to the maximum wave amplitude (“damping + noise”). Two different methods were tested for calculating the slopes of edge segments in the spatiotemporal images: (i) using only start and end points (“pp”) or (ii) a linear fit of all segment points (“lf”). The influence of 2-D median filters on wave velocity images was examined with no filtering (“no”) or filtering with different window sizes (“3 × 3”, “5 × 5” and “7 × 7”).

between 1% (without damping) and 4% (with damping). Here, additional noise has no determinable influence.

An incremental increase to a 7 × 7 window size for the 2-D median filter leads to a continuous increase in the calculated shear wave velocities. For a 7 × 7 median filter without damping, the increase in the shear wave velocity is 8% (pp) and 4% (lf). With damping, the rise is 5% (pp) and 4% (lf), and with additional noise 7% (pp) and 4% (lf).

Regarding the deviation angles, errors for the cases without damping, with damping and for damping with additional noise (no median filtering applied) are 3.3° (pp)/3.6° (lf), 6.4° (pp)/5.5° (lf) and 6.7° (pp)/6.4° (lf), respectively. In the absence of damping, a minimum deviation angle of 1.2° is found for filter sizes of 5 × 5 using the linear fit method. In the presence of damping, a minimum deviation angle of 1.1° is observed for filter sizes of 7 × 7 and the pp method. With additional noise, the minimum deviation is about 1.4° for a 7 × 7 filter and the pp method. For damped waves, a combination of the linear fit method

and 7 × 7 median filtering provides the best overall agreement between specified and calculated values of shear wave velocity and wave propagation direction independent of the presence of noise.

The results on the influence of reflections on the algorithm are listed in Table 2. The maximal relative error of the determined shear wave velocity was -13.5% in the investigated cases. None of the simulations had negative slopes in the spatiotemporal images.

3.2. Results for in vivo MRE of the human brain

Deflection patterns of brain tissue with motion components in transversal, coronal and sagittal directions could be found by visual inspection of the 2-D wave images (Fig. 8(a)–(c)). In our experimental setup, the head made a combined right-to-left and tilt movement. For this motion mode, the largest penetration depth of shear waves into the brain tissue was found for motion encoding in the anterior–posterior direction, corresponding to the u_x -deflection (Fig. 8(a)–(c)). Here, mechanical waves propagate congruent to the shape of the brain surface from the skull and the meninges into the brain. The largest deflection amplitudes in all directions were found in parts of the cerebrum and the cerebellum adjacent to the tentorium cerebelli. The effective damping was obvious from the strong decrease in shear wave amplitude with increasing penetration depth toward the center of the brain (see Fig. 8(d)).

Quantitative analysis of the $u_x(x, y, z, t)$ deflection field provides a mean shear modulus μ of 3.5 kPa ($1.7 < \mu < 6.1$ kPa) in the direction of the wave propagation. This average over gray and white matter is calculated assuming

Table 2
Relative error intervals for shear wave velocities caused by reflection

	Shear modulus (kPa)		Reflection coefficient	Relative error of shear wave velocity (%)
	Gray	White		
Green et al. [24]	2.8	2.1	-0.07	-1.7 to +2.6
Uffman et al. [23]	12.9	15.2	+0.04	-2.6 to +3.8
Kruse et al. [19]	6.4	14.6	+0.20	-12.0 to +12.0
McCracken et al. [25]	5.3	10.7	+0.17	-13.5 to +4.3

Data are given for four cases of impedance differences between white and gray matter from the literature. A density of 1000 kg m⁻³ was assumed for brain tissue to calculate the reflection coefficients for the interfaces between gray and white matter.

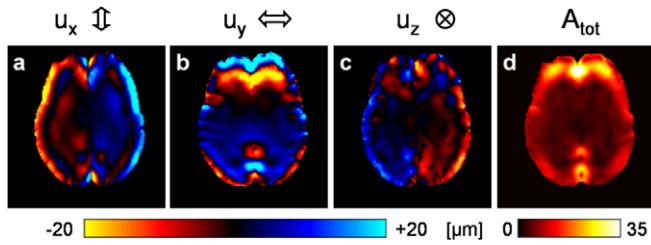


Fig. 8. Examples of wave images and the corresponding total amplitude image (A_{tot}) for an image slice in transversal orientation. Depicted here are the three orthogonal deflection components in anterior–posterior (u_x), left–right (u_y) and head–feet (u_z) directions (acquisition parameters: TE 124 ms, TR 2 s, FoV 192×192 mm, 6 mm slice thickness, and 1.5×1.5 mm in-plane resolution). The total amplitude image was calculated by $A_{\text{tot}} = \sqrt{A_x^2 + A_y^2 + A_z^2}$ (phase coherence between the deflection components was assumed). Amplitude images of the components A_x , A_y and A_z were determined by temporal Fourier transformation for each deflection component.

a density of 1000 kg m^{-3} for brain tissues and corresponds to a mean shear wave velocity of about $1.88 \pm 0.58 \text{ m s}^{-1}$.

Analysis of the variation between the direction of wave propagation and the orientation of the main image planes

revealed parabolic variation for the averaged deviation angles $\bar{\alpha}_{\text{trans},j}$, $\bar{\alpha}_{\text{cor},j}$ and $\bar{\alpha}_{\text{sag},j}$. These deviations showed minima near the center and a strong increase toward the outer regions of the brain (Fig. 9(a)–(c)). The minimum deviation angles were 17.0° for transversal, 12.5° for coronal and 28.3° for sagittal slices with standard deviations between 5° and 25° . Deviation angles of up to 75° were found for the outer regions. On the basis of the observed averaged deviation angles of 12.5° up to 75° , overestimation factors for the shear modulus between 1.05 and 15 were calculated using Eq. (9). The correlation of overestimation factor and deviation angle is shown in Fig. 9(d).

Slabs limited in thickness by a relative error of 10% in shear modulus overestimation were defined parallel to transverse, coronal and sagittal image planes. The corresponding overestimation factors were 5–15.5%, 9.4–20.4% and 29–41.8%. The slab thicknesses were 48 mm, 51 mm and 21 mm in the transversal, coronal and sagittal orientations, respectively (Fig. 10). For the slice of Fig. 8(a), an averaged shear modulus of about 4.4 kPa was calculated using the Helmholtz inversion technique. The ray analysis for the corresponding surface points yielded an average

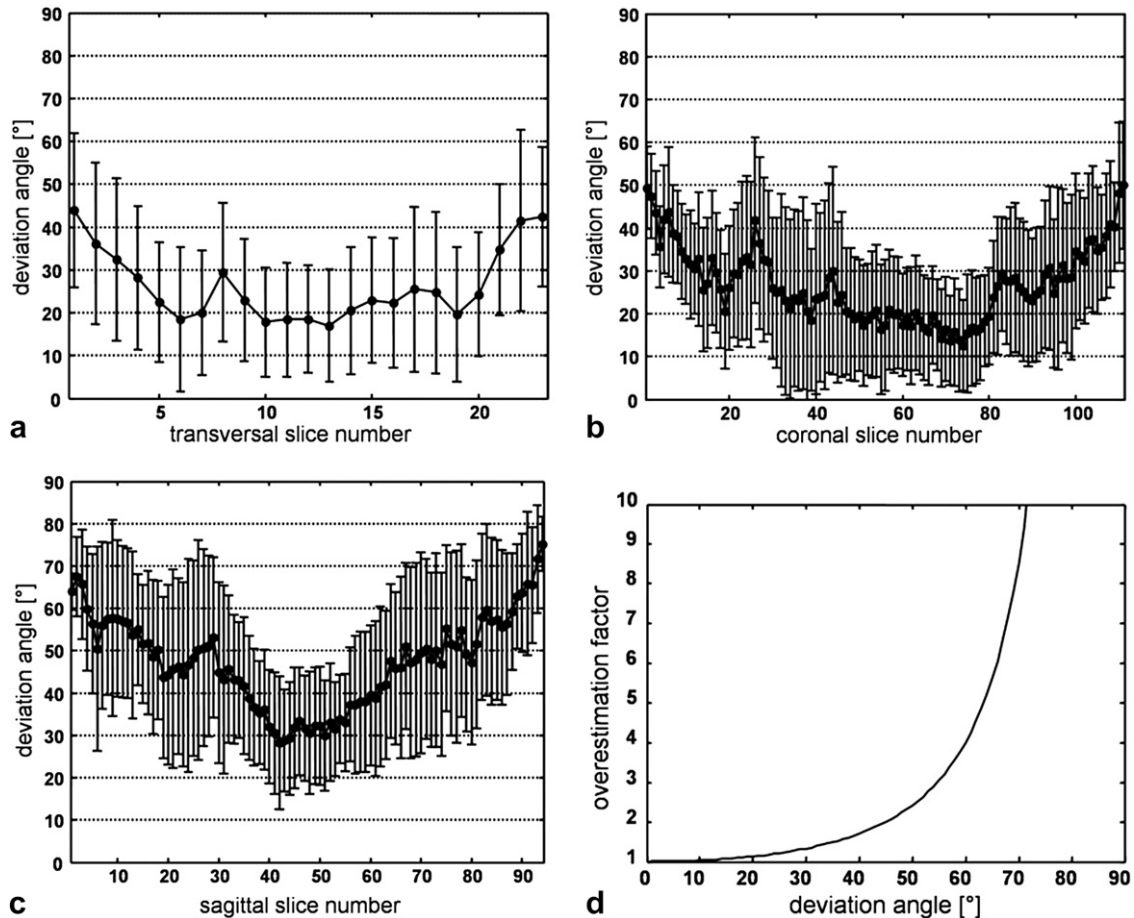


Fig. 9. Shear wave velocity and direction of wave propagation. Deviation angles were averaged over respective slices and plotted against the corresponding slice numbers for (a) transversal, (b) coronal and (c) sagittal orientations and ordered from foot to head (transversal, 1–23), anterior to posterior (coronal, 1–111) and left to right (sagittal, 1–94). The number of slices differs due to (i) the varying spatial resolution given in the image planes and the slice number and (ii) the geometry of the brain. (d) Overestimation factor of the shear wave velocity against the deviation angle between the direction of wave propagation and its projection on the image plane.

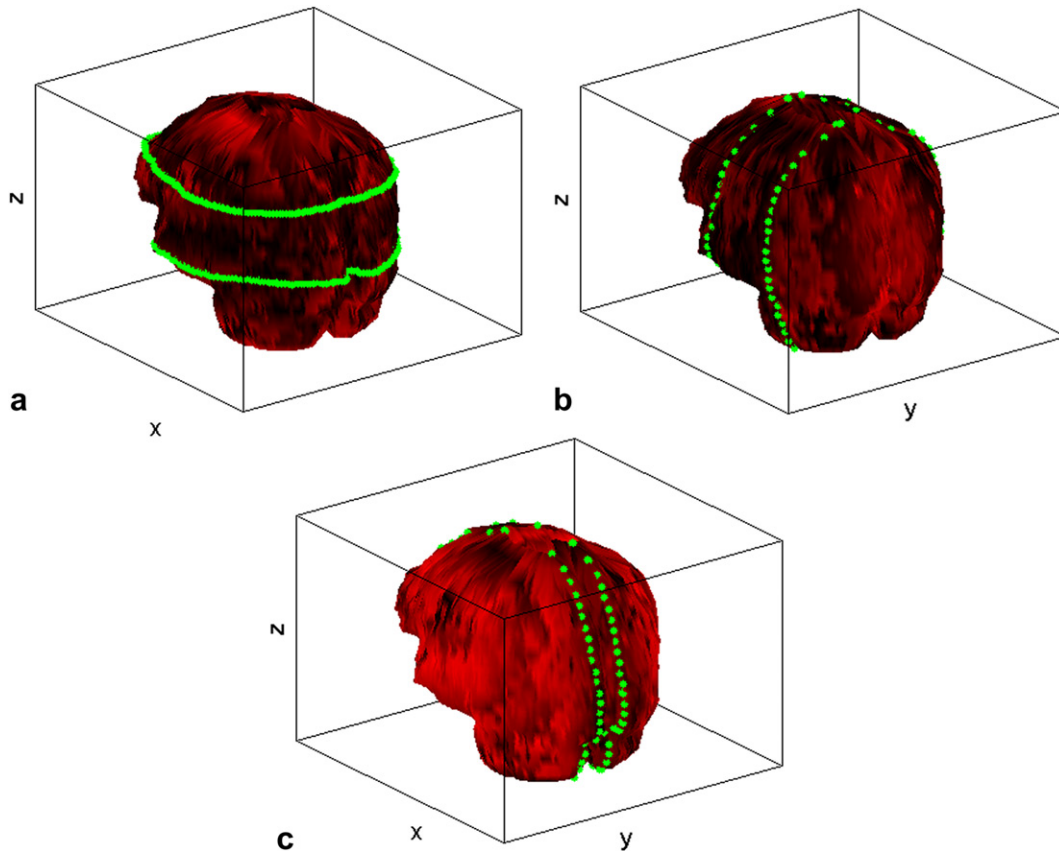


Fig. 10. Deviation angles visualized on the 3-D brain surface. Deviations are color encoded and range from dark red (0°) to bright red (90°). Regions between discrete surface points were interpolated. Slabs with a 10% relative error in the overestimation factor for the shear modulus are defined in (a) transversal, (b) coronal and (c) sagittal directions by green dots. Elasticity reconstruction is possible in these regions using inversion techniques with single-wave images; errors range between 5% and 42%.

shear modulus of about 3.7 kPa. The 1.18 times higher inversion-based shear modulus was in good agreement with the overestimation factor of 1.14 resulting from an average deviation angle of 20.5° for the wave propagation relative to the image slice.

4. Discussion

Verification of the accuracy of the proposed method was done using software phantoms comparable in size, damping properties, signal-to-noise ratio and spatial resolution to *in vivo* MRE data of the brain. Variable program parameters were analyzed to optimize the method for application to *in vivo* MRE data.

Specifically, application of the linear fit procedure yielded clearly better results than calculations based on start and end points of edge segments in spatiotemporal images. This can be explained by the higher number of data points taken into account in the linear fit. In both methods, damping leads to a slightly altered edge detection. This is caused by the Canny algorithm, which is sensitive to the intensity distribution of the data. An amount of noise comparable to that found in *in vivo* MRE data of the brain has, independent of filtering, only a minor influence on the sim-

ulation results. An explanation for this behavior may be the fact that the interpolation performed to obtain the deflections at the exact positions of the analyzed rays acts like a filter and leads to a certain amount of smoothing.

The application of median filters with increasing window size causes an increase of the minimal shear wave velocity and the corresponding standard deviation. In the presence of the damping that occurs in experimental MRE data of the brain, this effect can compensate for the underestimation of shear wave velocity by the linear fitting of edge segments.

The simulation of spatiotemporal images with reflections was based on published data on the elastic properties of living brain determined with MRE. Subsequent simulations of position-dependent interferences of incident and reflected waves yielded a maximal relative deviation of -13.5% from the specified shear wave velocity. However, an error of about 4% resulting from the data of Green et al. [24] and Uffmann et al. [23] seems more likely. No negative slopes were detected in the simulations. Reflections resulted in only slight changes of the segment slopes in the spatiotemporal image. This leads to the assumption that negative slopes only occur if the back-traveling wave is dominant, which seems very unlikely considering the published data.

Taking these observations into account, we considered only segments with positive slopes in spatiotemporal images for the *in vivo* data. Further reasons supporting this approach are (i) the fact that we focused on the detection of waves traveling from the surface into the brain, and (ii) the inherent limitations of the image-based edge-detection algorithm, which may in some cases find edges that are not physically plausible.

Except for the central part of the brain where the shear wave amplitude is strongly reduced by damping, experimental wave images showed the presence of motion patterns with non-negligible shear wave amplitudes in all spatial directions (Fig. 8). This observation can be interpreted in terms of effects comprising (i) the transfer path of mechanical motion into brain tissue, (ii) the complex shape and (iii) the anatomy of the brain. Less is known about the mechanism of mechanical excitation of brain tissue. A causal relationship between the shearing of the brain surface and the shape of the tentorium cerebelli is thought to be responsible for the high deflections in this region. A comparable influence of meninges was seen in the region of the falx cerebri (Fig. 8(a)–(c)). Despite low-frequency mechanical excitation, strong damping led to a continuous attenuation of the shear wave amplitude, which results in a low signal-to-noise ratio in the inner regions of the brain. In experiments based on single-wave images and the use of bite bars, other groups obtained results that are in good agreement with the wave patterns presented in this work [23–25]. However, our findings prove the absence of planar shear waves propagating within image planes.

Despite the very fast EPI–MRE imaging acquisition technique presented, the complete 4-D wave field for three orthogonal motion components of the brain with a spatial resolution of $1.5 \times 1.5 \times 6$ mm and 20 time points would take over 90 min to acquire. This is too long for practical application. In a first approximation, brain tissue was assumed to be isotropic. This enabled confinement to one component u_x of the deflection vector field $\vec{u}(x, y, z, t)$ and a reduction of the total acquisition time to about 30 min. The u_x component showed the best penetration of brain tissue. This was mainly determined by the motions produced by the particular actuator, which in our case was a mixture of a tilt-like and a left-to-right motion.

Before the shear modulus could be quantified, it was necessary to preprocess the 4-D data. For brain data, preprocessing comprised phase unwrapping and spatiotemporal filtering. Phase unwrapping was necessary because phase wraps may occur by mapping the imaged physical quantity on the interval $(-\pi, \pi]$. Spatiotemporal filtering ensured the extraction of shear waves with accurate frequency. A temporal band-pass filter selected only waves that propagated with the mechanical excitation frequency. Other frequencies, such as the natural vibrations of the brain, were filtered out. A 3-D spatial Butterworth band-pass filter was used to eliminate long-wave components and noise. Removing waves with very low wavelengths

can help to suppress compressional waves and bulk motion effects [9].

The data analysis was restricted to surface points of the segmented brain, although it would be possible to calculate wave propagation vectors for all data points. This restriction was made due to (i) the low ratio between the shear amplitude and the noise of the phase-difference images in deeper regions of the brain caused by the strong damping, and (ii) the prolonged computation time necessary for the calculation of multiple data points.

In contrast to commonly used inversion techniques, the method presented here relies on a temporal analysis of rays through the wave propagation field. The propagation and therefore the direction of shear waves can be detected because of the strong damping in the brain (see Fig. 8(d)). This prevents the development of standing waves which would inherently impede the determination of any wave propagation. Rays representing minimum shear wave velocities were assumed to point in the directions of wave propagation.

No distinction was made between gray and white matter. The reasons for this were: (i) the fact that shorter ray lengths cause increasing inaccuracy in determining the shear wave velocity because the reduced number of data points and the resulting errors do not allow for the differentiation between the small elasticity difference of white and gray matter; and (ii) the small extension of gray matter compared to the shear wavelength.

The rays were limited to a length of 3.75 cm. This length corresponded to about 1.5 shear wavelengths, which approximately matched the visually observable penetration depth. Thus, brain tissue located close to the center of the brain was excluded from the analysis to avoid errors in the edge-detection process in regions characterized by a low ratio between shear wave amplitude and noise.

The average shear modulus of 3.5 kPa is valid for an excitation frequency of 83.33 Hz. The comparison of frequency-dependent results obtained for a single slice with the proposed ray-based algorithm and a 2-D inversion technique yielded higher values for the shear modulus determined by inversion. This can be explained by the overestimation due to the deviation angle between the direction of wave propagation and the orientation of the image slice. If this overestimation is compensated for, the shear moduli determined with the different methods show good agreement, which proves the applicability of our method.

Compared to shear moduli of 2–3 kPa given by Green et al. [24], who used a 3-D inversion algorithm, our values are somewhat higher. This small discrepancy may be explained by the influence of viscosity, which, in contrast to our approach, was incorporated into their analysis. Regarding results published for single-slice data acquired at comparable excitation frequencies and elasticity reconstruction using inversion methods (assuming isotropy and absence of damping) [19,23], the shear modulus given in the present work is distinctly lower. These differences may be explained by the mismatch between wave

propagation and slice orientation. It was shown that the overestimation of the shear modulus varied between 1.05- and 15-fold depending on the image position.

However, slabs defined by a relative error of 10% in shear modulus overestimation existed for transverse, coronal and sagittal image orientations (Fig. 10). Thus, 2-D inversion techniques can be applied in these regions to single-wave images with relatively small errors in the calculated shear modulus. This opens up the possibility of reducing the measuring time to less than 2 min (1 slice, 20 time points per wave cycle) provided that the experimental setup and especially the mode of mechanical excitation are kept unchanged. Given these restrictions, MRE examinations could even be applied in patients with brain diseases. If pathologies are located outside these regions, a 3-D inversion must be done, which entails a longer acquisition time.

All elasticity reconstruction techniques based on strongly idealized physical modeling of mechanical waves have certain prerequisites to ensure successful application to MRE data. Regarding the proposed algorithm, which shows a minor sensitivity to noise, these prerequisites are ideally the absence of reflections and a lack of wave interference. However, the reflections have only a moderate influence on the results, as shown by the simulations and discussed already in the context of the simulated data. This holds true for the elastic properties of the human brain. For other organs and tissues characterized by less damping and larger differences in shear stiffness, the applicability of the proposed algorithm must be carefully re-evaluated.

The existence of interfering shear waves must likewise be carefully examined. With the given mode of mechanical excitation, the data analysis showed shear wave propagation with large deflection amplitudes close to the skull, in frontal and occipital regions of the cerebrum, and in areas close to the meninges. Hence superpositioning of mechanical waves will most likely occur in the frontal and occipital parts of the brain hemispheres. The amplitude of mechanical excitation has to be balanced with the damping, which helps to prevent superpositioning of mechanical waves.

5. Conclusions

Our results show that quantitative data for *in vivo* elastic properties of brain tissue can be obtained by combining an EPI–MRE acquisition technique with analysis of the propagating 3-D wave fields. The proposed method uses the effective direction of the shear wave propagation to calculate the shear modulus. A position-dependent overestimation of the shear modulus was demonstrated for inversion techniques on the basis of single-wave images. This was due to a mismatch between the image orientation and the direction of shear wave propagation.

Since the acquisition time is still about 35 min when using the very fast EPI–MRE technique assuming isotropy, a tradeoff between accuracy and acquisition time must be

made before the technique is applied in patients. The smallest possible shear modulus overestimations of 5–29% were deduced for transversal, coronal and sagittal slices located near the center of the brain. In these regions, fairly reliable values for shear modulus can be calculated from single-wave images using 2-D inversion algorithms. This approach reduces the measurement time to less than 2 min and even allows MRE examinations of patients with brain diseases.

Acknowledgement

The project was supported by the Deutsche Forschungsgemeinschaft (Br 2235/2-1, Sa 901/3-1).

Appendix A. Supplementary data

Supplementary data associated with this article can be found, in the online version, at [doi:10.1016/j.actbio.2006.08.007](https://doi.org/10.1016/j.actbio.2006.08.007).

References

- [1] Muthupillai R, Lomas DJ, Rossman PJ, Greenleaf JF, Manduca A, Ehman RL. Magnetic resonance elastography by direct visualization of propagating acoustic strain waves. *Science* 1995;269(5232):1854–7.
- [2] Muthupillai R, Rossman PJ, Lomas DJ, Greenleaf JF, Riederer SJ, Ehman RL. Magnetic resonance imaging of transverse acoustic strain waves. *Magn Reson Med* 1996;36(2):266–74.
- [3] Bishop J, Poole G, Leitch M, Plewes DB. Magnetic resonance imaging of shear wave propagation in excised tissue. *J Magn Reson Imaging* 1998;8(6):1257–65.
- [4] Van Houten EE, Paulsen KD, Miga MI, Kennedy FE, Weaver JB. An overlapping subzone technique for MR-based elastic property reconstruction. *Magn Reson Med* 1999;42(4):779–86.
- [5] Sinkus R, Lorenzen J, Schrader D, Lorenzen M, Dargatz M, Holz D. High-resolution tensor MR elastography for breast tumour detection. *Phys Med Biol* 2000;45(6):1649–64.
- [6] Oliphant TE, Manduca A, Ehman RL, Greenleaf JF. Complex-valued stiffness reconstruction for magnetic resonance elastography by algebraic inversion of the differential equation. *Magn Reson Med* 2001;45(2):299–310.
- [7] Hamhaber U, Grieshaber FA, Nagel J, Klose U. Illustration of elasticity differences using MR-elastography. *Z Med Phys* 2001;11(4):236–44.
- [8] Braun J, Buntkowsky G, Bernarding J, Tolxdorff T, Sack I. Simulation and analysis of magnetic resonance elastography wave images using coupled harmonic oscillators and Gaussian local frequency estimation. *Magn Reson Imaging* 2001;19(5):703–13.
- [9] Manduca A, Oliphant TE, Dresner MA, Mahowald JL, Kruse SA, Amromin E, et al. Magnetic resonance elastography: non-invasive mapping of tissue elasticity. *Med Image Anal* 2001;5(4):237–54.
- [10] Sinkus R, Tanter M, Catheline S, Lorenzen J, Kuhl C, Sondermann E, et al. Imaging anisotropic and viscous properties of breast tissue by magnetic resonance-elastography. *Magn Reson Med* 2005;53(2):372–87.
- [11] Hamhaber U, Grieshaber VA, Nagel JH, Klose U. Comparison of quantitative shear wave MR-elastography with mechanical compression tests. *Magn Reson Med* 2003;49(1):71–7.
- [12] Ringleb SI, Chen QS, Lake DS, Manduca A, Ehman RL, An KN. Quantitative shear wave magnetic resonance elastography: comparison to a dynamic shear material test. *Magn Reson Med* 2005;53(5):1197–201.

- [13] Vappou J, Willinger R, Breton E, Choquet R, Goetz C, Constantinesco A. Dynamic viscoelastic shear properties of soft matter by magnetic resonance elastography using a low-field dedicated system. *J Rheol* 2006;50(4):531–41.
- [14] Kemper J, Sinkus R, Lorenzen J, Nolte-Ernsting C, Stork A, Adam G. MR elastography of the prostate: initial *in-vivo* application. *Rofo-Fortsch Rontg* 2004;176(8):1094–9.
- [15] Kruse SA, Dresner MA, Ehman RL. MR elastography of human kidney *in vivo*: a feasibility study. In: Proceedings of ISMRM, Kyoto; 2004. p. 2600.
- [16] Rouviere O, Yin M, Dresner MA, Rossmann PJ, Burgart LJ, Fidler JL, et al. In vivo MR elastography of the liver: preliminary results. In: Proceedings of ISMRM, Miami, 2005; p. 340.
- [17] Huwart L, Peeters F, Sinkus R, Annet L, Salameh N, ter Beek LC, et al. Liver fibrosis: non-invasive assessment with MR elastography. *NMR Biomed* 2006;19(2):173–9.
- [18] Felmlee JP, Rossmann PJ, Muthupillai R, Manduca A, Dutt V, Ehman RL. Magnetic resonance elastography of the brain: preliminary *in vivo* results. In: Proceedings of ISMRM, Vancouver; 1997. p. 683.
- [19] Kruse SA, Dresner MA, Rossmann PJ, Felmlee JP, Jack CR, Ehman RL. “Palpation of the brain” using magnetic resonance elastography. In: Proceedings of ISMRM, Philadelphia; 1999. p. 258.
- [20] Braun J, Bernarding J, Tolxdorff T, Sack I. *In vivo* magnetic resonance elastography of the human brain using ultrafast acquisition techniques. In: Proceedings of ISMRM, Honolulu; 2002. p. 2597.
- [21] Moore DF, Pursley R, Dimitriadis E, Talagala SL. Magnetic resonance imaging of brain transverse acoustic waves. In: Proceedings of ISMRM, Toronto; 2003. p. 2298.
- [22] McCracken PJ, Manduca A, Ehman RL. MR elastography for studying the biomechanics of traumatic brain injury. In: Proceedings of ISMRM, Toronto; 2003. p. 799.
- [23] Uffmann K, Maderwald S, Greiff Ad, Ladd ME. Determination of gray and white matter elasticity with MR elastography. In: Proceedings of ISMRM, Kyoto; 2004. p. 1768.
- [24] Green M, Sinkus R, Bilston LE. High resolution 3D brain MR-elastography. In: Proceedings of ISMRM, Seattle; 2006. p. 2021.
- [25] McCracken PJ, Manduca A, Felmlee J, Ehman RL. Mechanical transient-based magnetic resonance elastography. *Magn Reson Med* 2005;53(3):628–39.
- [26] Weaver JB, Van Houten EEW, Miga MI, Kennedy FE, Paulsen KD. Magnetic resonance elastography using 3D gradient echo measurements of steady-state motion. *Med Phys* 2001;28(8):1620–8.
- [27] Papazoglou S, Rump J, Braun J, Sack I. Shear wave group velocity inversion in MR elastography of human skeletal muscle. *Magn Reson Med* 2006;56(3):489–97.
- [28] Schmitt F, Stehling MK, Turner R. Echo-planar imaging: theory, technique and application. Berlin: Springer; 1998.
- [29] Ghiglia DC, Pritt MD. Two-Dimensional phase unwrapping – theory, algorithms, and software. New York: Wiley Interscience; 1998.
- [30] Kovsi P. Edge linking and line segment fitting, 2001–2005. <http://www.csse.uwa.edu.au/~pk/Research/MatlabFns/index.html>.